eng

MDPI

Article

Fabrication of Black Silicon Antireflection Coatings to Enhance Light Harvesting in Photovoltaics

Klodian Dhoska [1,*], Evjola Spaho [2] and Uljan Sinani [3]

[1] Faculty of Mechanical Engineering, Polytechnic University of Tirana, Square Mother Theresa No. 1, 1019 Tirana, Albania
[2] Faculty of Information Technology, Polytechnic University of Tirana, Square "Mother Theresa" No. 4, 1019 Tirana, Albania; espaho@fti.edu.al
[3] Department of Biomedical Engineering, University of Reading Whiteknights, P.O. Box 217, Reading Berkshire RG6 6AH, UK; u.sinani@pgr.reading.ac.uk
* Correspondence: kdhoska@fim.edu.al

Abstract: Black silicon has attracted significant interest for various engineering applications, including solar cells, due to its ability to create highly absorbent surfaces or interfaces for light. It enhances light absorption in crystalline solar cells, improving the efficiency of converting incident light into electricity for photovoltaic applications. This research focused on fabricating nanostructures that played a critical role in enhancing light absorption in the upper layers of solar cells. These nanostructures were created using the black silicon method, forming a layer known as "black silicon". The coating not only improved the efficiency of crystalline solar cells but also enhanced their stability. The antireflection coating, composed of nanostructures with various shapes, including conical, pillar-like, and spike-like forms, achieved a reflectivity as low as 10% in the spectral range of 400–700 nm. This corresponded to a sample with $\alpha = 0.85$ and a chuck bias of 4 W. An Inductively Coupled Plasma Reactive Ion Etching (ICP RIE) machine was employed to develop and control the specific shape, size, and density of the fabricated black silicon, which was then subjected to testing. The efficiency of the black silicon photovoltaic cell was 23.3%.

Keywords: black silicon; antireflection coating; solar cells; inductively coupled plasma reactive ion etching

Citation: Dhoska, K.; Spaho, E.; Sinani, U. Fabrication of Black Silicon Antireflection Coatings to Enhance Light Harvesting in Photovoltaics. *Eng* **2024**, *5*, 3358–3380. https://doi.org/10.3390/eng5040175

Academic Editor: Qiuwan Shen

Received: 22 November 2024
Revised: 9 December 2024
Accepted: 10 December 2024
Published: 14 December 2024

1. Introduction

The use of renewable energy sources such as wind, solar, etc., has been growing rapidly worldwide to reduce greenhouse gas emissions and mitigate climate change [1–4]. High demand for renewable energy, particularly solar energy, has driven significant advancements in silicon solar cell technologies for efficient energy harvesting. Today, silicon-based solar cells dominate the commercial market, accounting for approximately 80% of production. This prevalence is attributed to silicon's abundance, cost-effectiveness, and well-established fabrication methods [5–7]. As the second most abundant element on Earth, silicon plays a crucial role in semiconductor technology, microelectronics, and nanotechnology. Its widespread availability, coupled with mature manufacturing processes, makes it indispensable for applications requiring high efficiency, flexibility, and cost-effectiveness, such as optoelectronics, photonics, biosensors, and semiconductor devices [7–13]. Furthermore, silicon-based composite materials have been employed as self-cleaning surfaces, reducing efficiency losses in solar cells, lowering cleaning costs, and maintaining surface stability [14–18]. Recently, alongside the development of deterministic fabrication techniques, a wide range of self-organized methods for creating silicon nanostructures have emerged [19–24]. Additionally, one of the primaries focuses in photovoltaic technology has been the use of black silicon (b-Si) in solar cells [25].

Research on the properties of b-Si is still relatively new and widening. However, its potential for solar cells is rapidly being exploited [26]. Black Si solar cells achieved a high conversion efficiency as well as lower costs compared to conventional crystalline Si solar cells [27,28]. In comparison to other silicon solar cells, such as those with dielectric coatings like SiNx, b-Si offers broader spectral effectiveness in reducing reflection across a wide range of wavelengths. This is particularly evident in the UV, visible, and near-infrared spectra, where SiNx can only be optimized for specific wavelengths, particularly in the visible range [29]. Furthermore, b-Si solar cells can significantly improve light absorption in the top layer, offering a potential solution to the challenges faced by current designs [29,30]. In our case, we tried to exploit the properties of silicon as an element using special etching techniques to produce nanostructures used in solar cells and increase efficiency [31].

According to the literature, the field of nanotechnology has recently evolved exponentially to achieve higher resolutions at the nanoscale using different methods and techniques. Recent developments in nanotechnology, particularly lithography, have enabled the creation of nanoscale features with unprecedented precision. Lithography methods are being developed to transfer even smaller features into substrates [4]. Techniques such as Extreme Ultraviolet Lithography (EUV) [31], Electron Beam Lithography (EBL) [31,32], and Nano Imprint Lithography (NIL) [33], combined with precise thin-film deposition methods, facilitate the fabrication of microelectronic devices at the nanometer scale. Many of these structures, produced using methods such as vapor–liquid–solid (VLS) growth or wet-chemical catalytic etching, are commonly referred to as "silicon nanowires", whereas structures created through dry etching are typically known as "black silicon" [19,20]. With advancements in these processes, etching techniques such as Inductively Coupled Plasma Reactive Ion Etching (ICP RIE) have also evolved, becoming essential for the precise construction and control of multilayer patterns [34]. Additionally, the ICP RIE technique was employed to fabricate black silicon nanostructures for solar cell applications. Based on different attempts at nanostructure formation, the etching method offers several advantages, including precise nanostructuring, low reflectivity levels in the 400–700 nm spectral range, the ability to produce a variety of surface textures, and improved photovoltaic conversion efficiencies. Additionally, ICP RIE enhances the long-term stability of solar cells and reduces recombination losses, contributing to improvements in overall performance efficiencies. Based on these findings, the plasma etching method was chosen for its speed, precision, and superior controllability compared to conventional grating techniques [35]. Utilizing reactive species generated in plasma via a radio frequency (RF) electric field, this method enables the controlled formation of nanostructures with specific shapes and dimensions.

This paper presents the fabrication and characterization of black silicon antireflection coatings for solar cell applications. The uniqueness of this research lies in the combination of gas ratio optimization, advanced geometrical control, and the integration of superhydrophobicity, all of which contribute to improved optical properties and enhanced light trapping. These innovations are positioned as advancements over traditional black silicon fabrication methods [25–35]. The coatings consisted of nanostructures in various shapes, including conical, pillar-like, and spike formations, which were fabricated using Inductively Coupled Plasma Reactive Ion Etching (ICP-RIE) technology. The shapes, sizes, and densities of the black silicon nanostructures were characterized using Scanning Electron Microscopy (SEM). Reflectivity tests, the Bosch process, and water contact angle (WCA) measurements were conducted to evaluate the performance of the fabricated structures. The efficiency of a b-Si photovoltaic cell was determined by calculating the fill factor and total efficiency.

2. Experimental Setup and Measurements

Integrating black silicon into the photovoltaic cell fabrication process requires a sequence of steps designed to maximize light absorption and minimize recombination losses. Therefore, an effective passivation layer is essential to reduce recombination losses. This process begins with surface texturing, where techniques like reactive ion etching (RIE) are

used to create a highly textured, black surface. Plasma etching systems have been designed to prioritize either reactive chemical components or ionic components for better results (see Figure 1).

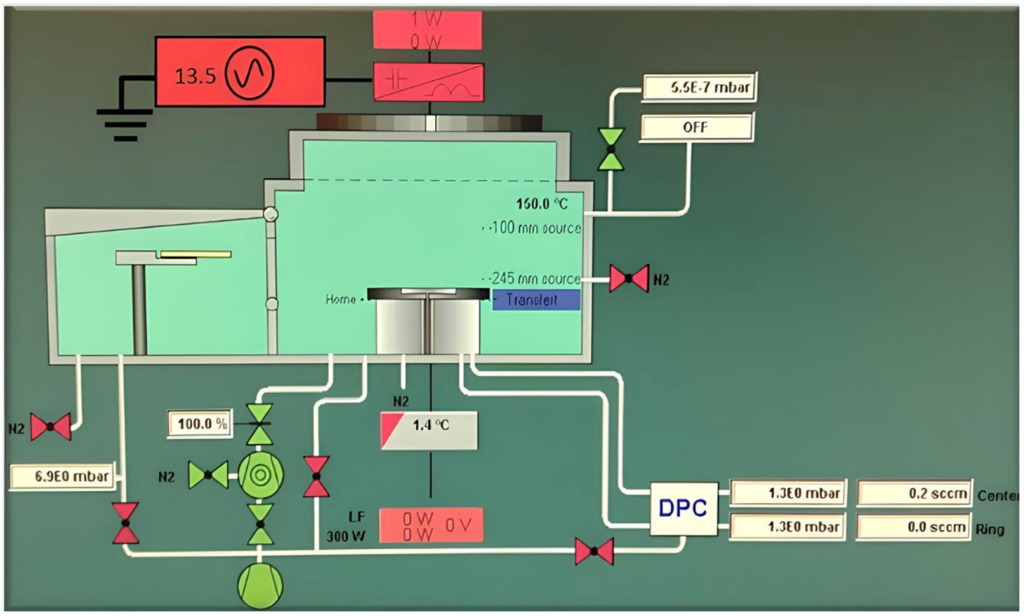

Figure 1. Inductively Coupled Plasma Reactive Ion Etching (ICP RIE) machine (NanoSYD) [36].

This method uses SF_6 and O_2 gases to generate fluorine (F*) and oxygen (O*) radicals. O* is responsible for forming a passivation layer of SiO_xF_y, while F′ etches silicon, producing volatile products like SiF_x. The passivation layer, assisted by oxygen, is partially removed through ion bombardment. The remaining uncovered silicon is then etched by F*. The etching reaction is exothermic, reducing the likelihood of forming a new passivation layer, as SiO_xF_y primarily results from desorption during heating. At this point, it is worth mentioning that the reaction occurs in the plasma system according to Equations (1)–(3) [37]:

$$Si + 4F = SiF_4 \quad (1)$$

$$Si + 2O = SiO_2 \quad (2)$$

$$SiO_2 + 4F = SiF_4 + O_2 \quad (3)$$

This reaction governs the competition between the etching and passivation processes, leading to the formation of random silicon microstructures. To control the morphology of black silicon (b-Si), various reactive ion etching (RIE) parameters have been optimized. These include the gas composition, flow rate, system temperature, substrate bias, and RF power, among others, each contributing to different morphological changes. Increasing the O_2 flow rate enhances the deposition of the passivation layer, while an increase in SF_6 flow promotes a more volatile reaction with silicon. By adjusting these parameters, the coverage, the passivation layer, and the density of the nanostructures can be controlled, with substrate bias playing a key role in influencing these characteristics during the RIE process.

In the fabrication process of b-SI, a range of devices were employed for sample handling, inspection, and data acquisition. Key tools included an SEM and an ICP RIE system. Additionally, WCA measurements were conducted to evaluate the hydrophobicity of the black silicon surface, including samples processed using the Bosch technique [36–40]. All ICP RIE plasma etching procedures were carried out in a Class 100 cleanroom environment, utilizing appropriate chemicals and tools to minimize contamination risks [39,41]. Nanostructural analysis of the fabricated samples was subsequently performed using SEM. Afterward, spectrometric analysis was conducted outside the cleanroom environment to

measure reflectivity and absorption. Figure 2 provides an overview of the experimental setup stages used in the fabrication of black silicon.

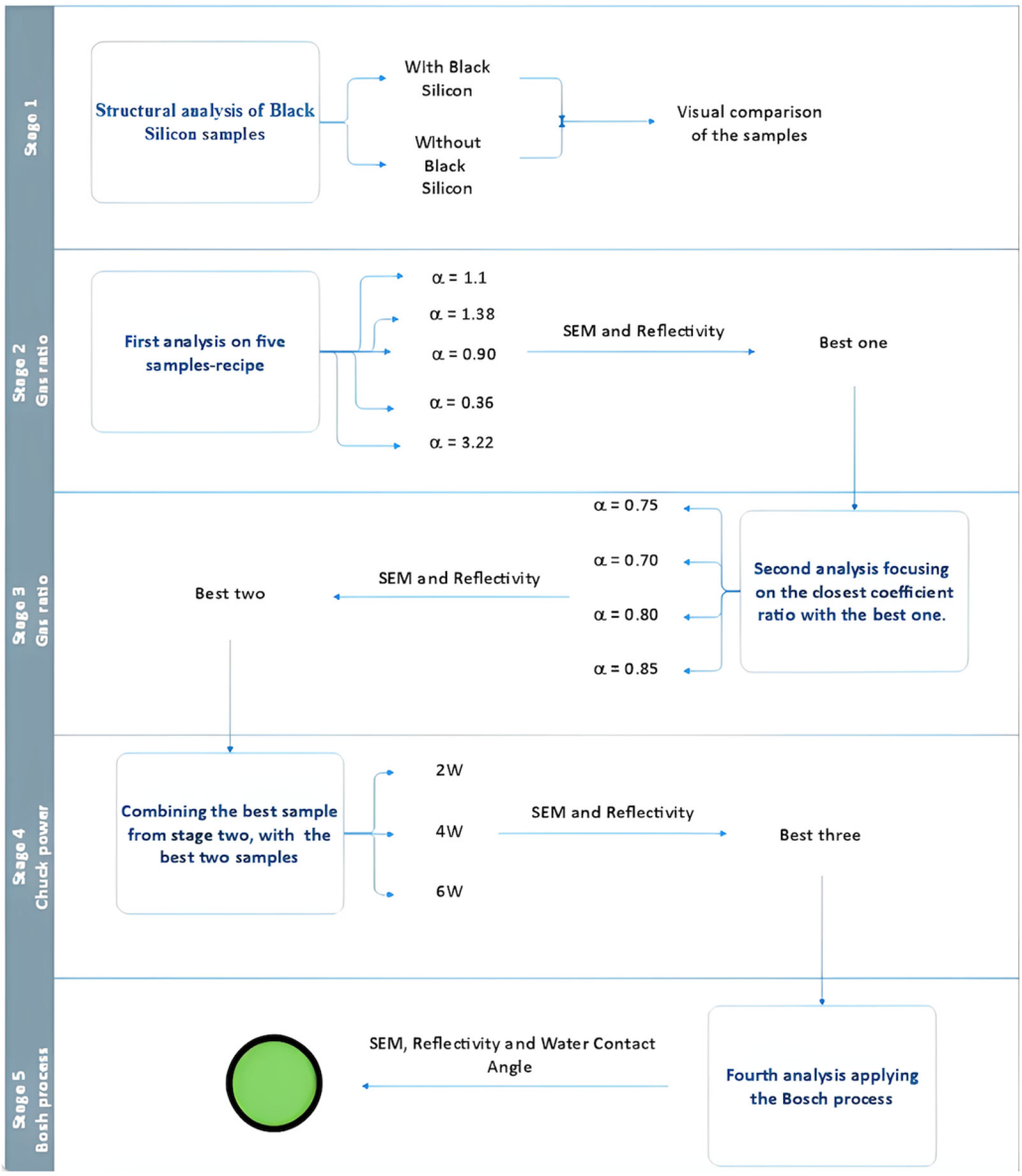

Figure 2. Experimental setup stages of the fabrication of black silicon.

In the initial stage of this research work, black silicon was fabricated on a clean silicon wafer using a plasma machine. The objective was to examine differences at the microstructural level and evaluate the behavior of black silicon on the surface of a raw silicon wafer. The first samples were created by varying the gas ratio of SF_6 and O_2 in the ICP RIE machine, guided by reference values from previous studies on black silicon [34]. Subsequent samples were fabricated using gas ratios similar to the initial ones, with feedback from the results informing adjustments to the next recipe, as can be seen in Figure 3.

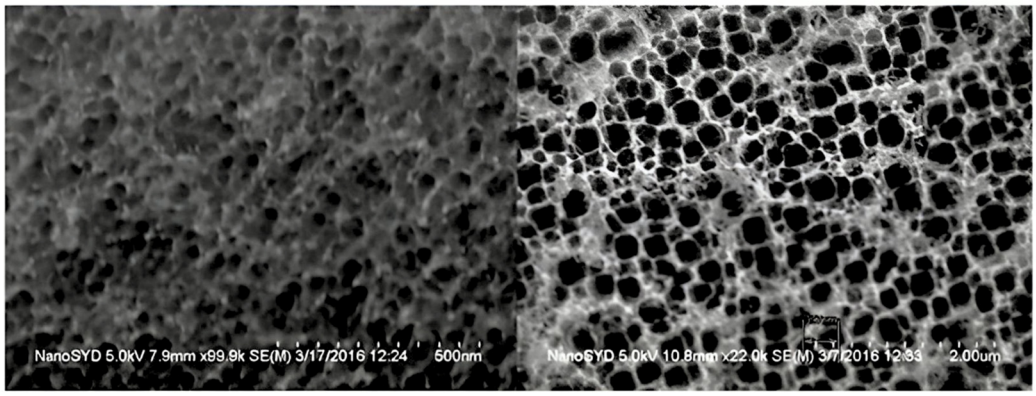

(**a**) (**b**)

Figure 3. (**a**) Poor black silicon and (**b**) a descent sample.

In the early stages of black silicon characterization, sample selection was initially based on the quality of the SEM images, followed by reflectivity measurements. The criteria for SEM analysis focused on the regularity of the microstructures, as well as the size and density of the holes, which are key factors influencing light scattering. As the process progressed, reflectivity measurements were added as additional criteria to aid in sample selection, streamlining the process.

It is important to note that during fabrication, some samples had to be reprocessed due to contamination or issues with thermal conductivity in the ICP RIE machine. To mitigate these issues, cleaned samples were prepared from raw silicon wafer cuts. After the cuts were made, the samples were placed in three separate beakers containing acetone, isopropanol, and distilled water. Each solution was applied for three minutes, and the samples were then dried by blowing air onto their surfaces. These samples were then subjected to further analysis in the ICP RIE machine.

The results and challenges encountered at each stage of the process are discussed in the following sections. The analysis begins with the test samples used to understand the properties of black silicon and measure feature sizes, which are compared with other samples. For each stage, the final sample results were stored and incorporated into later stages to refine the process and produce high-quality samples based on the original recipe. The accompanying images help illustrate the "surface nature" of each sample, reflecting the specific gas and power combinations used, which were the main variables in this process.

2.1. First Stage

In the first stage, a structural analysis of the black silicon was conducted, and SEM images were acquired to characterize the samples. The process was carefully documented with a focus on the geometric shapes and sizes of the microstructures formed on the silicon surfaces. This step aimed to understand how the gas ratio of SF_6 and O_2 influenced the geometry of the microstructures after the etching process.

The process began in the plasma machine, where only one variable was initially adjusted: the ratio of sulfur hexafluoride (SF_6) to oxygen (O_2). This ratio was set according to a recipe derived from previous research on black silicon [38,39]. Once the samples were prepared in the plasma machine, visual inspection via SEM was carried out. The images acquired during this inspection are shown in Figure 4. Only the recipe shown in Figure 4b, with a gas ratio of SF_6/O_2 = 100/90, resulted in successful black silicon formation. The other recipes, which used twice as much SF_6 or O_2, produced poor results, as seen in Figure 4c, which closely resembled the untreated samples shown in Figure 4a.

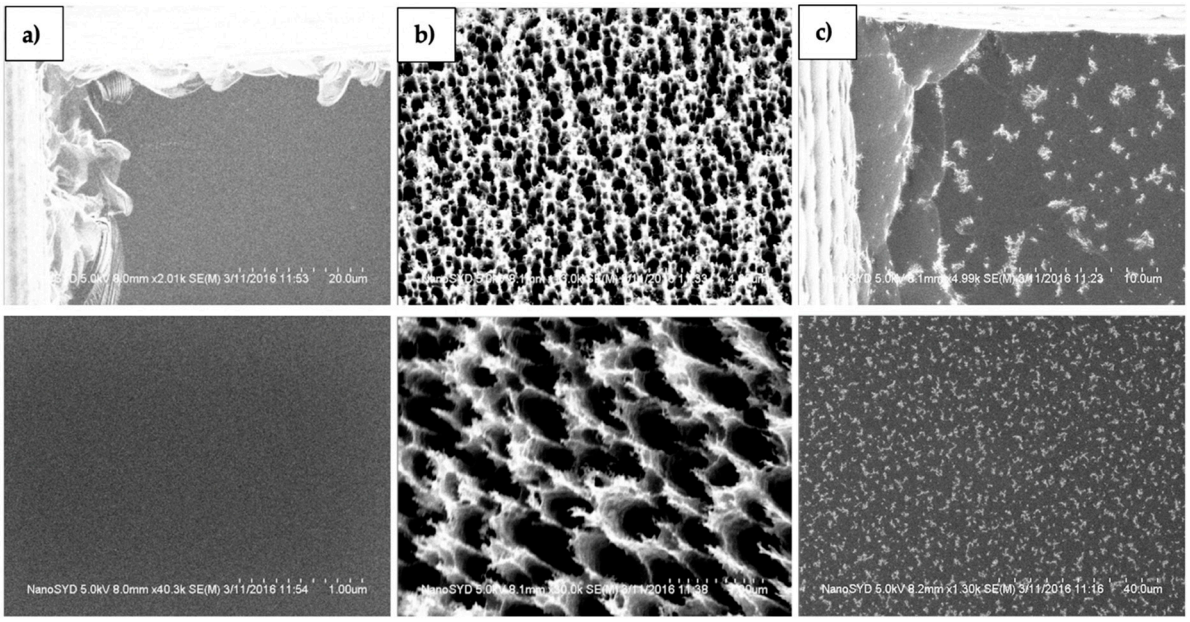

Figure 4. (**a**) Untreated silicon sample, (**b**) treated black silicon sample, and (**c**) poorly treated sample.

2.2. Second Stage

In the second stage, five samples were prepared and analyzed, following the steps outlined in the working schedule. One of these five samples was saved to serve as the basis for the next recipe in the following stage. The remaining samples underwent reflectivity testing, and ultimately, only the best-performing sample was selected for comparison in the later stages. The rationale for preparing five samples and selecting the best one was to identify the trends in the structures as the gas ratio changed according to an exponential function. This process began with the previous optimal recipe ($\alpha = 0.9$), and the gas ratio was adjusted by either increasing or decreasing the amounts of the gases in a manner that approximated an exponential law, aiming to optimize the recipe more efficiently. The results were based on SEM images of all samples treated with the gas ratios outlined in Table 1.

Table 1. The gas ratios derived from the recipe with a gas ratio of $\alpha = 0.9$ in the second stage.

Alpha SF_6/O_2	SF_6	O_2	O_2 Trend	SF_6 Trend
1.1	100	90	(reference)	(reference)
1.38	110	80	−10	+10
0.90	90	100	+20	−20
0.36	50	140	+40	−40
3.22	145	45	−95	+95

The SEM images from this stage are shown in Figure 5, where top and side views of five samples, along with reflectivity data, are shown.

Based on the top-view SEM images, the best samples, with a gas ratio of $\alpha = 0.9$, exhibited more regular structures, and the hole shapes were more circular. After analyzing the top-view images based on the criteria of regularity, size, and shape, a similar assessment was conducted on the side-view images, which were obtained after cutting the samples with a diamond tip. The sample with $\alpha = 0.9$ proved to be the best in terms of structural regularity. For further details, the side-view images of all five samples are shown in Figure 6.

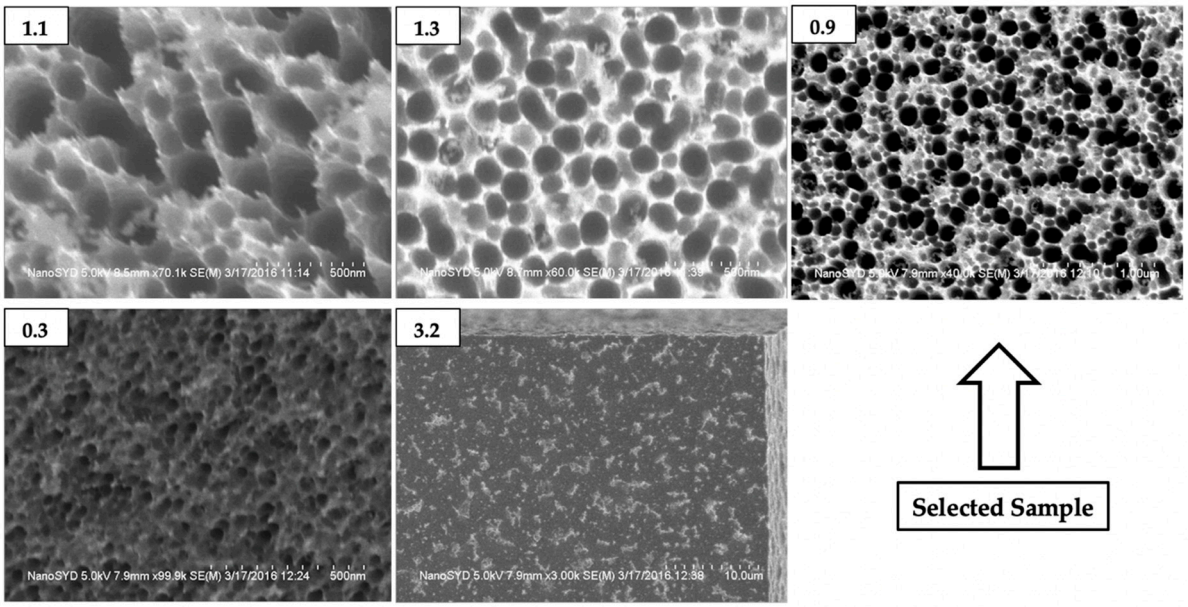

Figure 5. Top-view images of the samples derived from the main recipe.

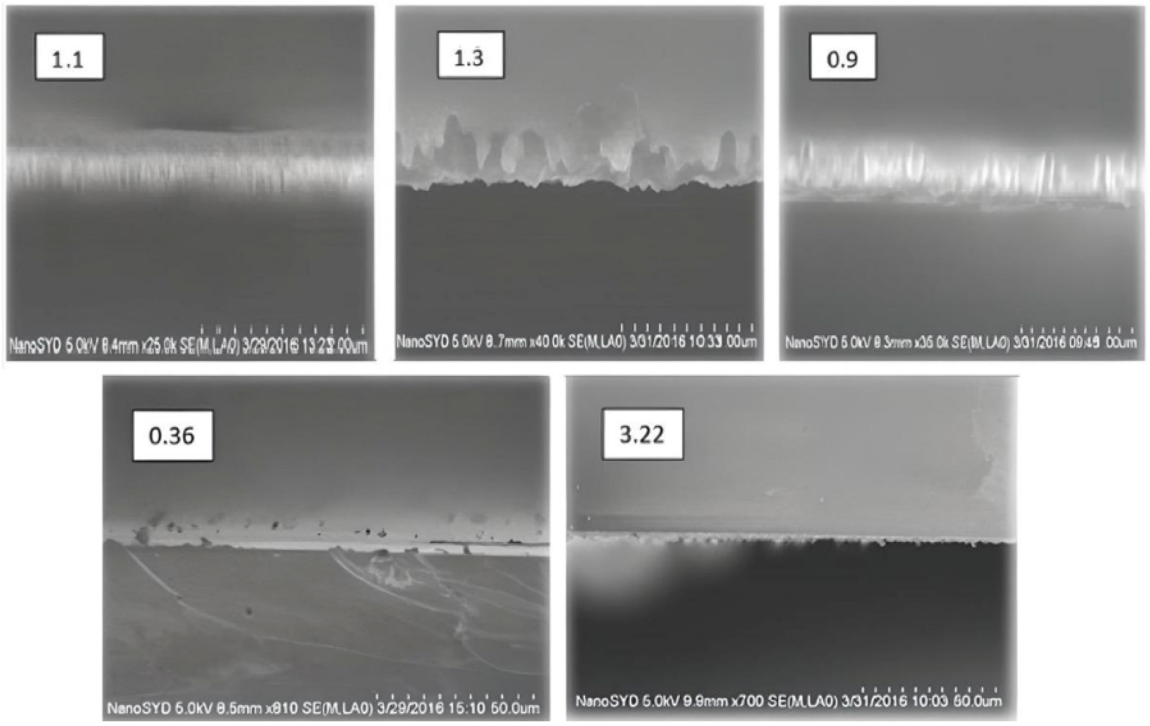

Figure 6. Side-view SEM images.

The side-view SEM images of the black silicon samples revealed that the sample with α = 0.9 exhibited the best nanostructures. This sample was identified as the most consistent. To further investigate the shapes and sizes of the pillars and the relationship between the pillars and light absorption rates, the images were used to measure the dimensions of the pillars. The results are presented in Figure 7.

Trenches No.	Height (nm)	Width (nm)
1	3.189	1.089
2	3.236	1.007
3	3.424	1.124
4	3.444	1.299
5	3.061	0.943

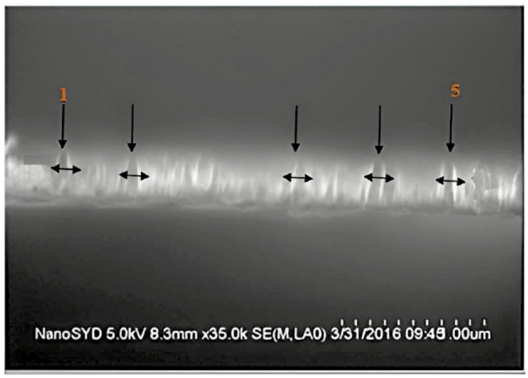

Figure 7. Geometrical size of the best sample (α = 0.9).

Following the SEM analysis, reflectivity measurements were conducted to quantitatively assess strategies for improving light absorption. Figures 8 and 9 illustrate the reflectivity measurement setup and the corresponding results for the optimal sample, respectively.

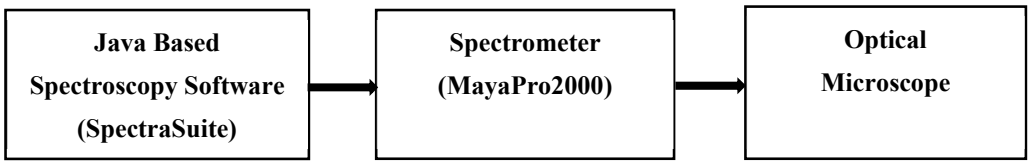

Figure 8. Reflectivity measurement setup.

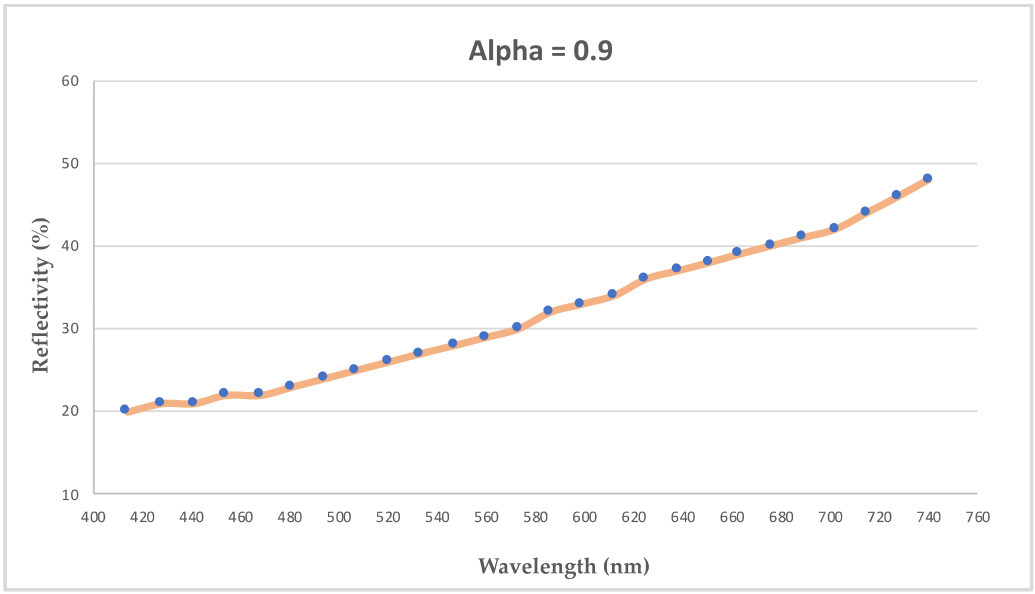

Figure 9. The reflectivity results for the best sample.

2.3. Third Stage

In the third stage, four new samples were derived from the best one (α = 0.9) during the first selection. Then, from this recipe, the two best samples were extracted, and SEM and reflectivity tests were performed. The 0.75 to 0.85 range was derived from a prior recipe that was shown to produce the best combination of the etching rate, surface structure, and material properties for photovoltaic cell efficiency. The gas ratios that were derived from the recipes are shown in Table 2.

The results obtained by SEM inspection of the top and side views after applying the derived recipes in the ICP RIE machine are shown in Figures 10–13.

Table 2. The gas ratios for the derived recipes in the third stage.

SF_6/O_2 Ratio	SF_6	O_2	
0.75	81.4	108.6	**Derived from recipes with α values of 1.1–0.9**
0.70	78.2	111.8	
0.80	84.4	105.6	
0.85	87.3	102.7	

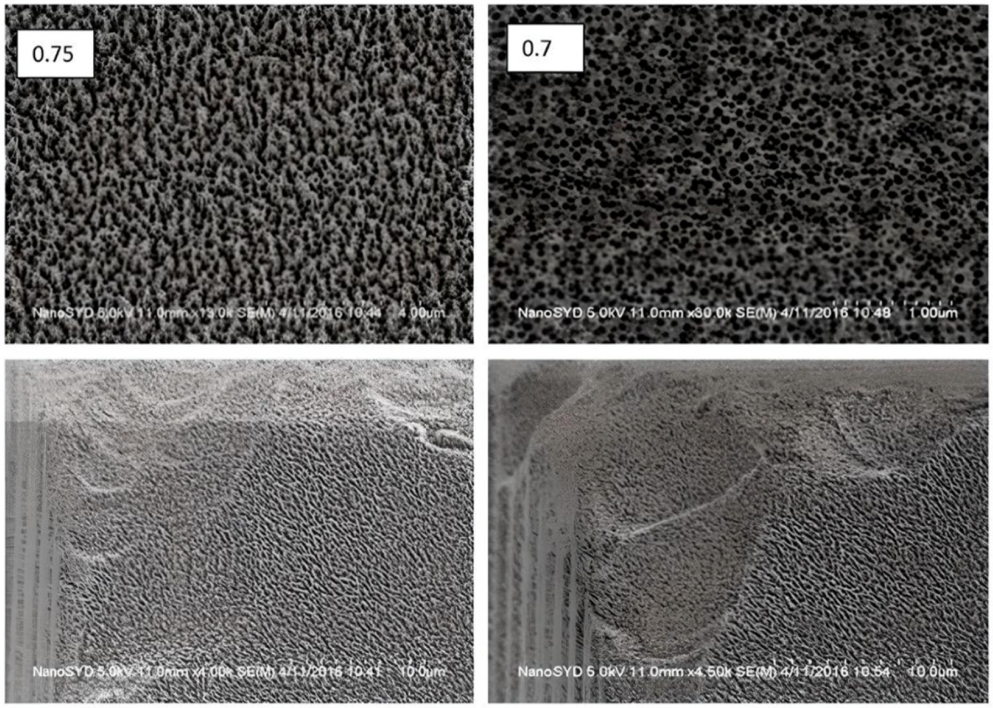

Figure 10. Top-view images for α = 0.7 and 0.75.

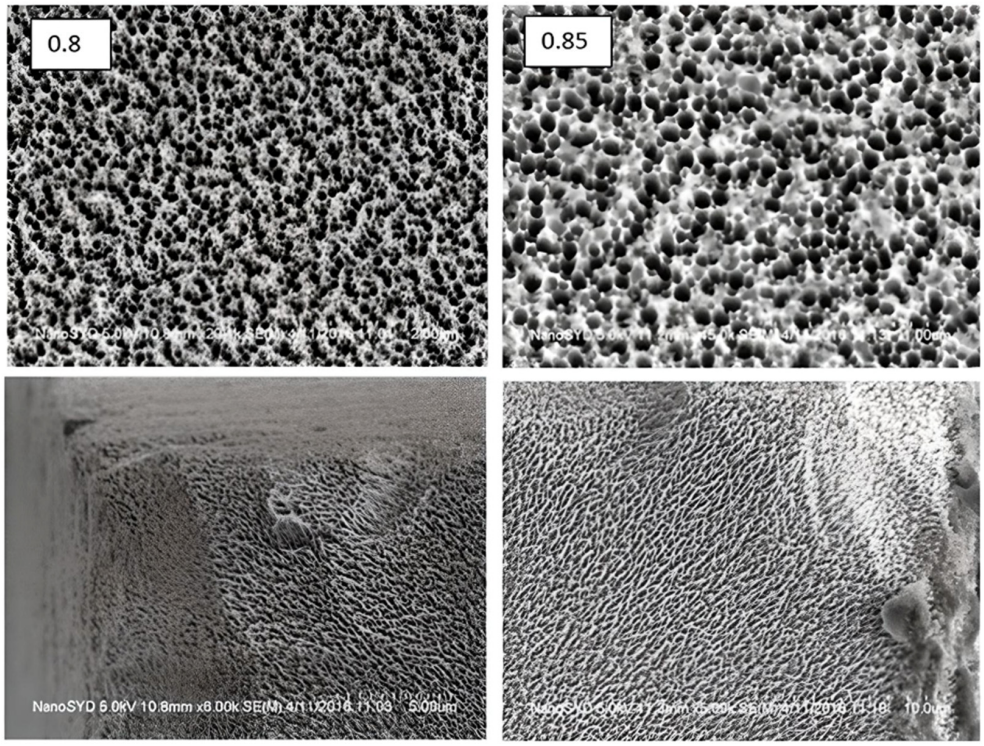

Figure 11. Top-view SEM images for α = 0.8 and 0.85.

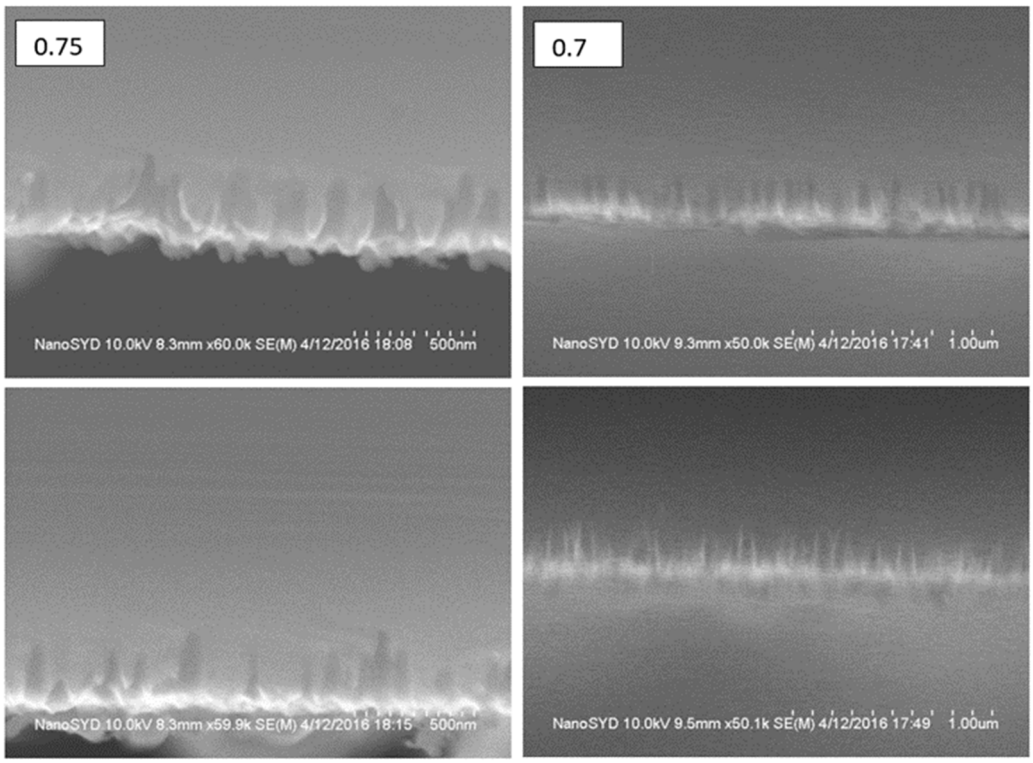

Figure 12. Side-view SEM images for $\alpha = 0.7$ and 0.75.

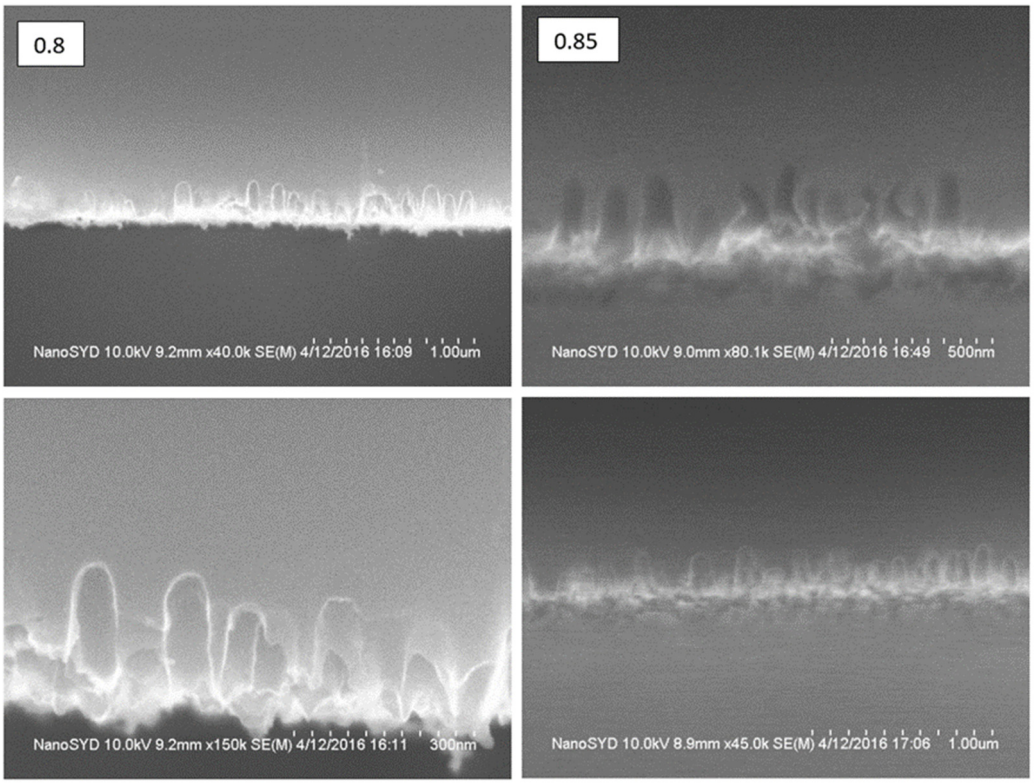

Figure 13. Side-view SEM images for $\alpha = 0.8$ and 0.85.

From the acquired SEM images, it is evident that in both cases the microstructure that was created (between the 'holes') was spread across the sample with the same density, and the size was roughly the same in all regions. For the sample with $\alpha = 0.75$, the structures were more regular and deeper, whereas in the right image of the sample with $\alpha = 0.7$ the

microstructures were poorer and not sharp. To compare these samples with the two other samples, another set of SEM images was taken, as shown in Figure 10. They were subjected to a reflectivity test, and combining both SEM and reflectivity data gave a better indication of which sample was best.

For the side view, the same procedure was carried out by cutting the samples after obtaining the top-view SEM images and comparing them based on features like the geometry of the grating, size, density, etc., for the reflectivity measurements.

Figure 11 shows the SEM images taken from the sides of the samples with lower ratios of $\alpha = 0.75$ and $\alpha = 0.7$. The difference in size between the pillars was very small. Furthermore, it was quite hard to determine which one had the lowest reflectivity rate.

In Figure 12, pillars 'coming out' of the surface can be seen, and the same result is shown when images from recipes with $\alpha = 0.8$–0.85 are combined. Since the gas ratio differences between the recipes were small, it was difficult to determine the best sample via visual inspection. But based on the reflectivity rate, the light absorption scale in the samples was more evident.

It is possible to see that the top- and side-view images of these samples are clearer, and the grating is more uniform across the area of each sample than between them. Based on the images taken from the side, some differences are evident in terms of the sizes and distributions of the trenches. Based on the images, it was quite difficult to judge which sample(s) was the best, so to avoid uncertainty when selecting the best sample, reflectivity measurements were performed.

Furthermore, the ratios of gases combined during the etching process resulted in different etching profiles due to the selectivity and dynamics of the process, influenced by the dominance or absence of one of the gases (either SF_6 or O_2). Having more O_2 in the system inhibited the etching process, thus increasing the SF_6 level to stabilize the process and make it etch the silicon surface.

In the opposite case, there was a high amount of SF_6 gas, which led to a situation where the passivation layer was not able to provide the micro masks necessary to form black silicon. For these reasons, the right equilibrium was theoretically easy to calculate, but in practice it was difficult to control, and it was difficult to understand the real variables acting during the etching process. At this stage, the reflectivity levels were quite close, as were the gas ratios (see Figure 14). All these considerations required analysis to choose the second-stage gas ratios to use for the next samples.

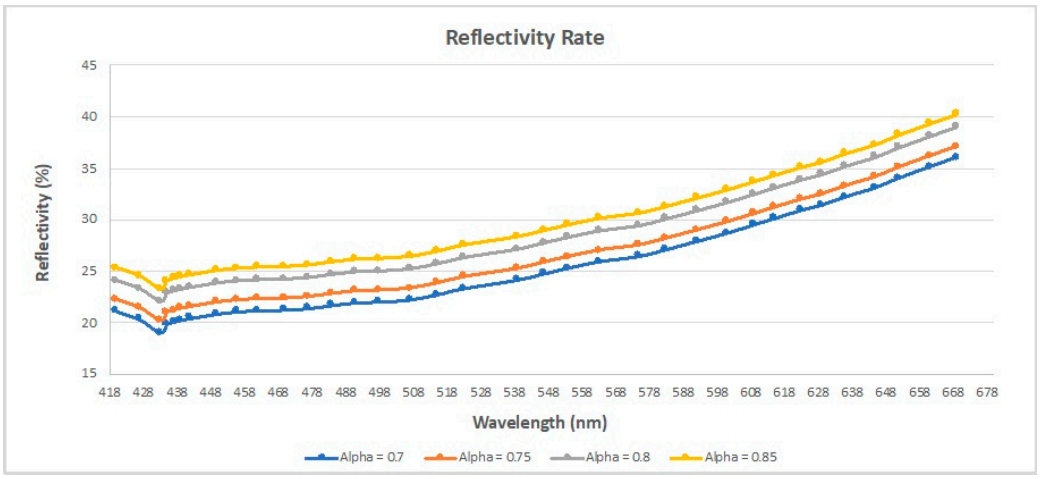

Figure 14. SEM reflectivity for $\alpha = 0.7$, 0.75, 0.8, and 0.85.

2.4. Fourth Stage

This stage of the work was carried out to find the best possible recipe to minimize the reflectivity level, and this stage introduced another variable to control: the chuck bias. The chuck bias, together with the gas ratio, contributed an additional change to the variables of

black silicon fabrication. The gas ratios that were derived from the recipes are shown in Table 3.

Table 3. Variables that were changed.

SF_6/O_2 Ratio	SF_6 (sccm)	O_2 (sccm)	Chuck Bias (W)	
0.75	81.4	108.6	2	**Derived from recipes with α values of 0.75–0.85**
	81.4	108.6	4	
	81.4	108.6	6	
0.85	87.3	102.7	2	
	87.3	102.7	4	
	87.3	102.7	6	

After all the recipes were executed with the ratios specified, including all the variables, it was possible to acquire the following images via SEM (Figures 15–18).

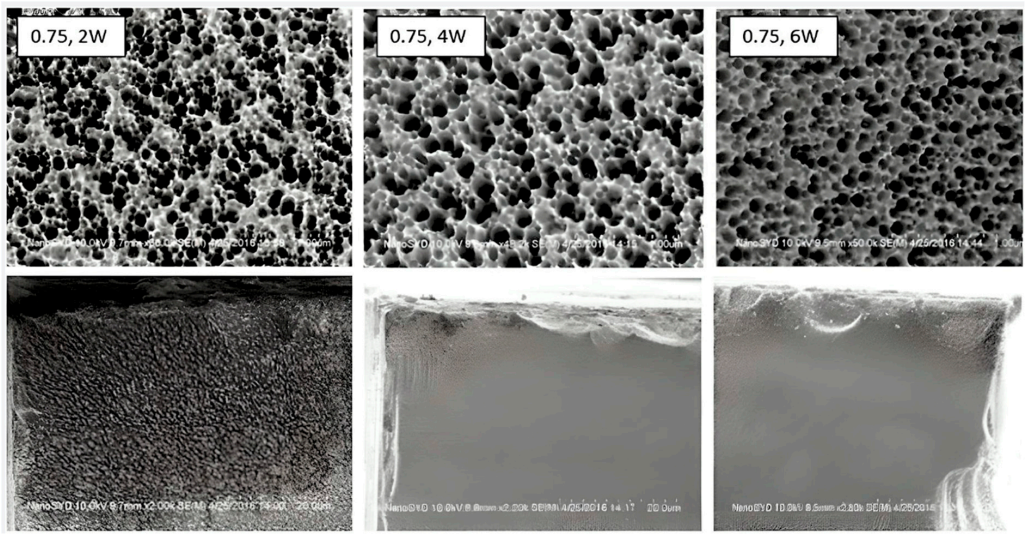

Figure 15. Top-view SEM images with different chuck bias powers.

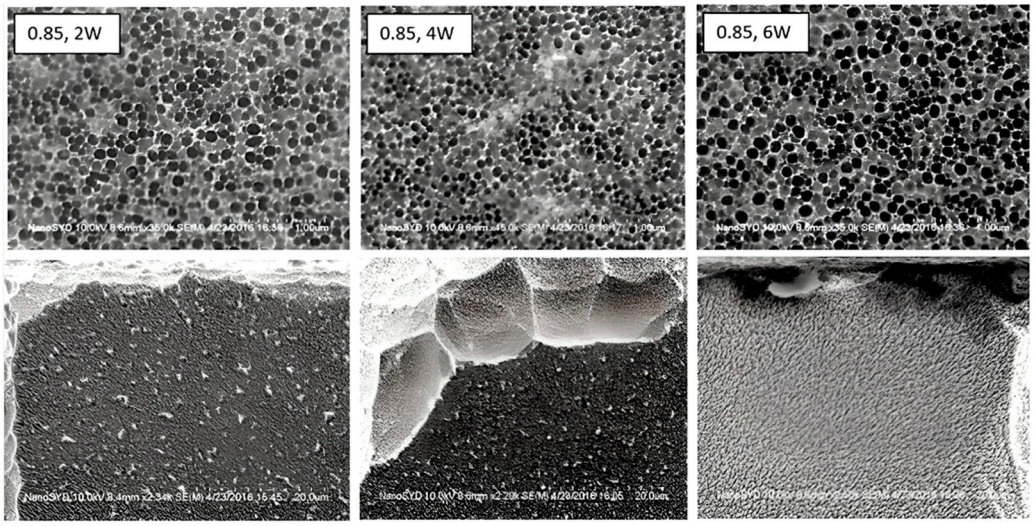

Figure 16. Top-view SEM images with different chuck bias powers.

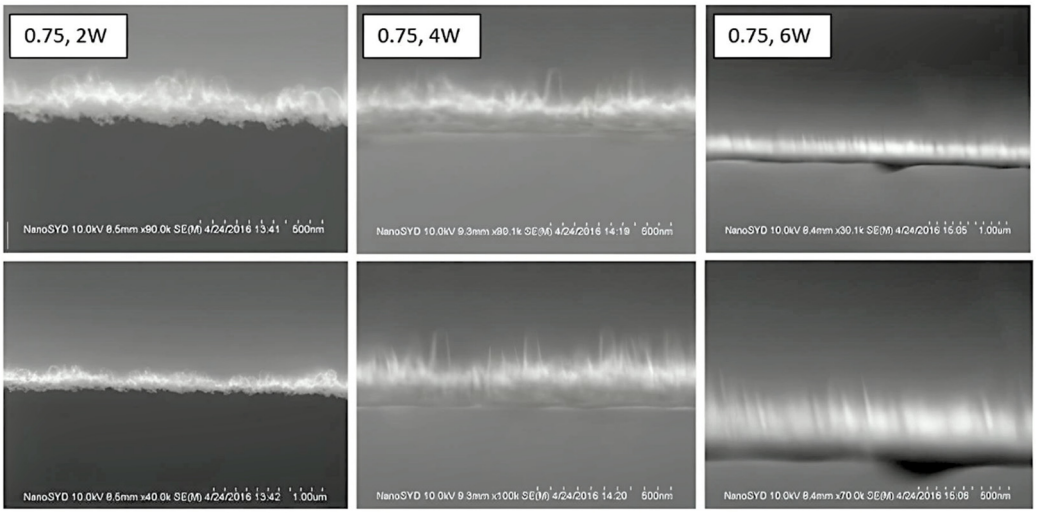

Figure 17. Side-view SEM images with different chuck bias powers.

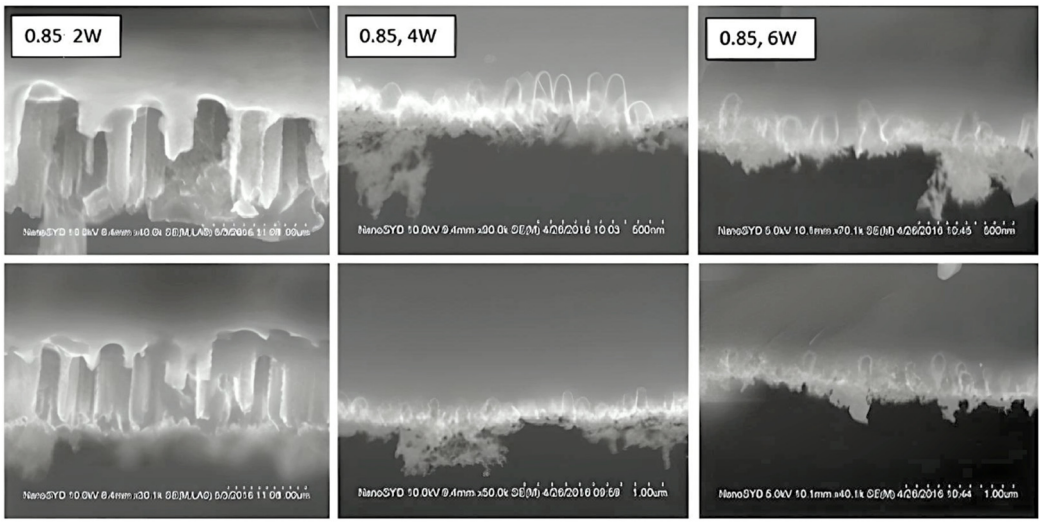

Figure 18. Side-view SEM images.

Figure 15 shows top-view SEM images of three samples with different bias power levels. Impurities can be observed in the samples, likely caused by ions impacting the surfaces and irregularities in the silicon crystal structures. Despite these imperfections, the pillar-like structures appear relatively regular at the 1 µm scale. However, it is difficult to determine from the top view alone which sample would exhibit the lowest reflectivity or the best light absorption rate.

Figure 16 presents the top views of samples with a gas ratio of $\alpha = 0.85$ that were treated at three different chuck bias power levels (2, 4, and 6 W). The microscale results for this second recipe set showed similar outcomes. Cracks and incomplete structures were visible at the corners of the samples, which sometimes complicated the acquisition of clear side-view images. Despite these issues, the top views still appeared similar across the samples.

Figures 17 and 18 display side-view images for each gas ratio combination. These images were taken under suboptimal conditions known as "static charge buildup", which caused blurriness due to interference with backscattered electrons. This affected the reflected electron energy, leading to image noise. However, despite the challenges, most of the side-view images still had acceptable quality for SEM analysis. Finally, the reflectivity data shown in Figures 19 and 20 provide a clearer understanding of the differences in the reflectivity levels across the samples.

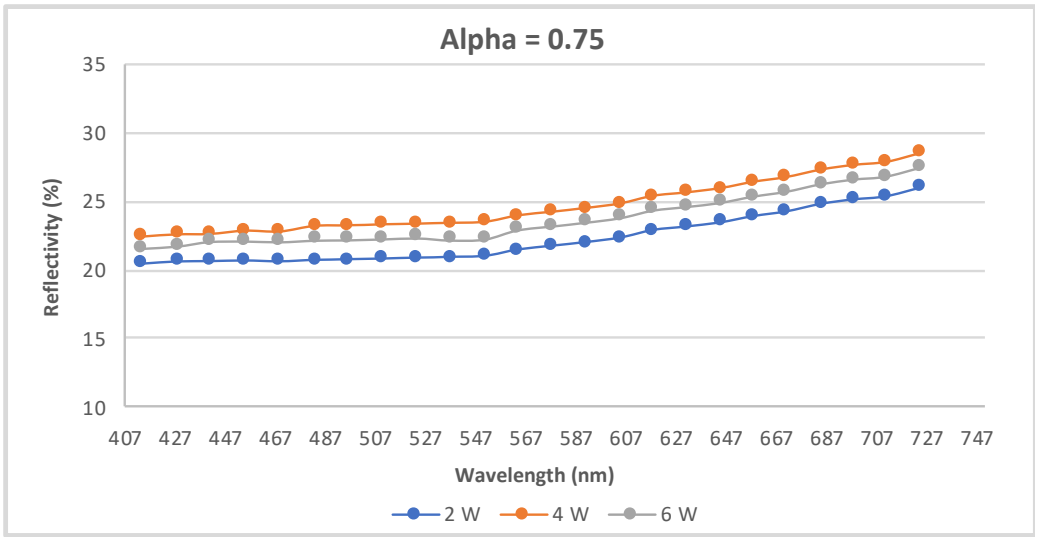

Figure 19. The reflectivity results across the samples.

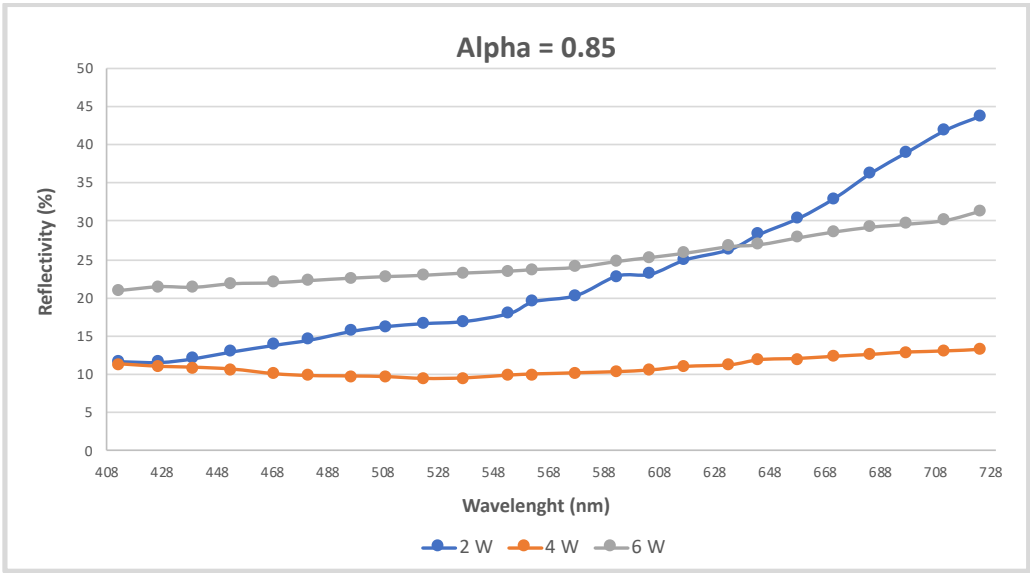

Figure 20. The reflectivity results across the samples.

Through the SEM image analysis, it was challenging to directly observe the variation in the reflectivity rates between the samples. However, the data obtained from the reflectivity tests clearly demonstrate a linear relationship for reflectivity across the wavelength range of 400–700 nm for each sample. The sample with $\alpha = 0.75$ and a chuck bias of 2 W exhibited the lowest reflectivity. The behavior of all three samples was consistent within the 400–700 nm wavelength range, and considering that the spectrometer's range spanned from 165 to 1100 nm, this stability in reflectivity is desirable, especially at lower reflectivity levels. Achieving such stability supports the goal of improving the reflectivity performance of black silicon.

Based on the reflectivity data, the best samples with the lowest reflectivity were those with $\alpha = 0.75$ and a chuck bias of 2 W, showing a reflection value of about 19% in the 400–500 nm range. The second best sample, as shown in Figure 19, was the one with $\alpha = 0.85$ and a chuck bias of 4 W, which achieved a reflectivity value around 10% in the 400–600 nm range, making it the selected sample. This sample demonstrated significantly lower reflectivity compared to the sample from the first set. Notably, both graphs show an improvement in light absorption after activating the chuck bias power.

The improvement in the reflectivity level can be attributed to the chuck bias power. When applied at lower power levels, it helps remove part of the passivation layer, enabling ions to etch deeper into the substrate. However, this also results in some loss of directionality in the etching process, leading to the formation of deeper and more irregular structures, as observed in the SEM images. Despite these irregularities, the pillars created by this etching process effectively trap incident light within the substrate, contributing to lower reflectivity levels.

2.5. Fifth Stage

After changing the chuck bias, the three best samples were selected based on the previous stages. In the last stage, an additional process, which was the Bosch process, took place. The plan was to treat the three best samples (two from the last recipe and one from the first) and observe any changes regarding the parameters of interest. The final recipe using the Bosch process was carried out with the sample ratios shown in Table 4.

Table 4. Gas ratio values.

SF_6/O_2 Ratio	SF_6 (sccm)	O_2 (sccm)	Chuck Power (W)
0.75	81.4	108.6	2
0.85	87.3	102.7	4
0.9	100	90	6

After applying these recipes in the ICP RIE machine, the new samples were sent directly into the Bosch process to see its effect at the microstructural level, according to the parameters shown in Table 4.

2.5.1. Bosch Process

In this step, after SEM and reflectivity testing, the three best samples out of nine were chosen. The top three samples were chosen after a selection process using Scanning Electron Microscopy images of the top and side views. Figure 21 provides a schematic view of the Bosch process.

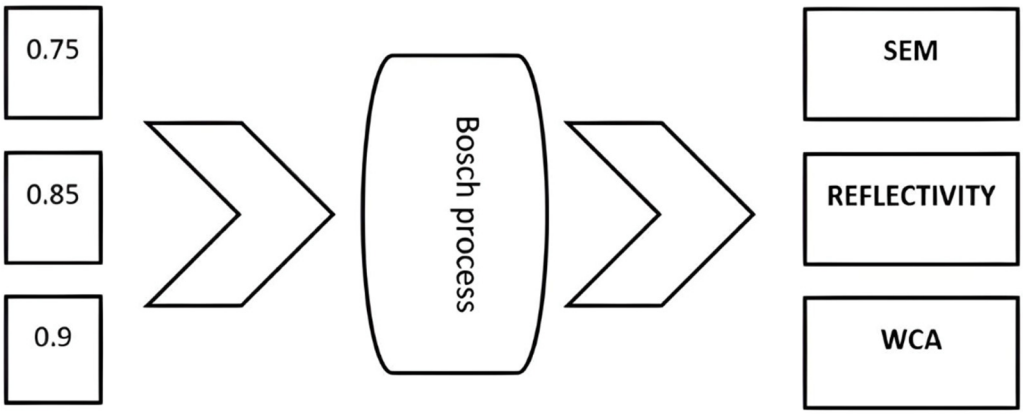

Figure 21. The Bosch process applied to the selected samples.

The Bosch process was applied after the best samples were chosen from the recipes with α = 0.75; 0.85; and 0.9. Then, the next steps were to test the results from the etching process in the ICP RIE machine with SEM and a reflectivity test. Another testing step, water contact angle (WCA) testing, was introduced to measure the hydrophobicity of the surfaces.

First, images were acquired via SEM for the top and side views. This time, they surprisingly showed evident differences. In the top view, all samples had size increases regarding the texture geometry, and from the side the pillars looked 'threaded' on the edges.

To provide a better understanding, an overview of the SEM images taken from the top and side is shown on the next page in Figures 22 and 23.

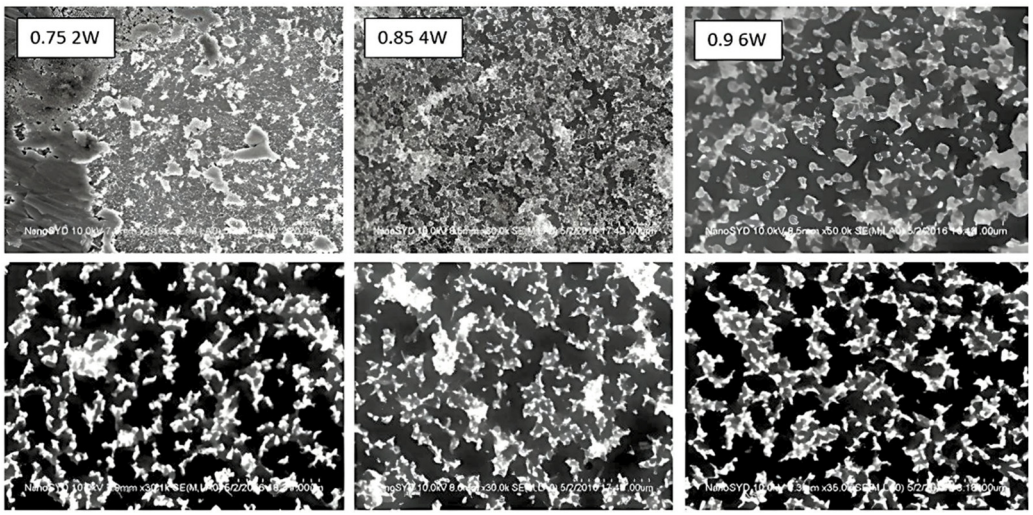

Figure 22. Top-view SEM images of the samples treated with the Bosch process.

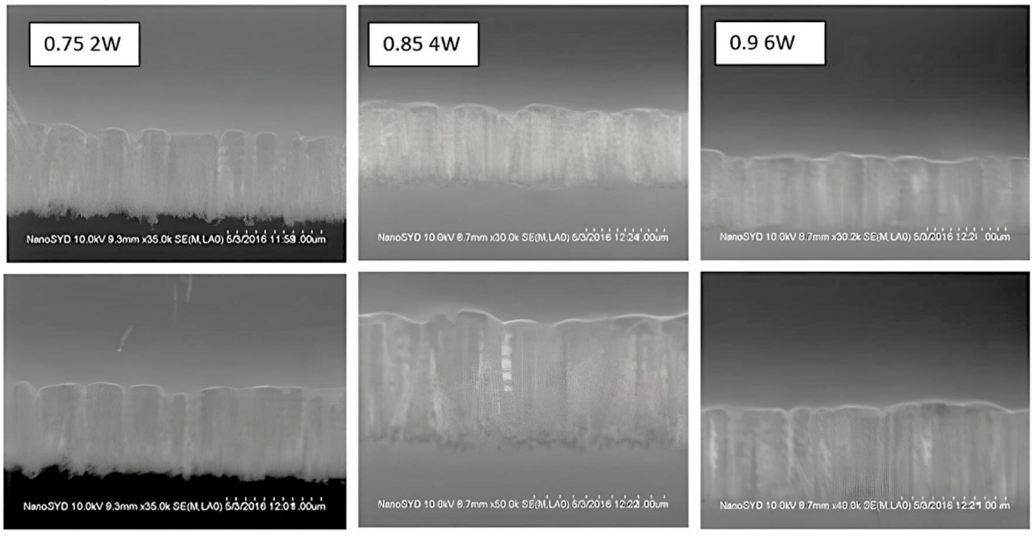

Figure 23. Side-view SEM images of samples treated with Bosch process.

In the side view, it was evident that the shape of the pillars had been improved, with a more uniform height distribution, which was ideal for achieving a higher level of hydrophobicity, as will be discussed later. Notably, the Bosch process had a significant impact on the structures: although the top-view images initially appeared irregular, the side-view SEM images revealed that the nanostructures (pillars) were, in fact, regular and uniformly distributed across the sample.

The top-view images demonstrate the effect of the etching process, which interacted strongly with the substrate, even within a short period of time. It is important to mention that the first test applying the Bosch process to black silicon lasted 30 s. After this test, the sample was essentially "wiped clean", with the nanostructures removed and the surface returned to its original smooth state. Following this, we reduced the duration of the Bosch process to 10 or 5 s. The etching results were more effective, and the nanostructures were preserved to a greater extent.

Figure 24 illustrates how the reflectivity levels changed dramatically when applying the Bosch process. In contrast to the previous samples, which exhibited reflectivity rates ranging from 10 to 20%, the absorption rate of these samples decreased significantly by

two to three times compared to the previous recipe. As a result, the reflectivity rate for the Bosch-treated samples was higher than expected, prompting us to perform the water contact angle (WCA) test as the next step.

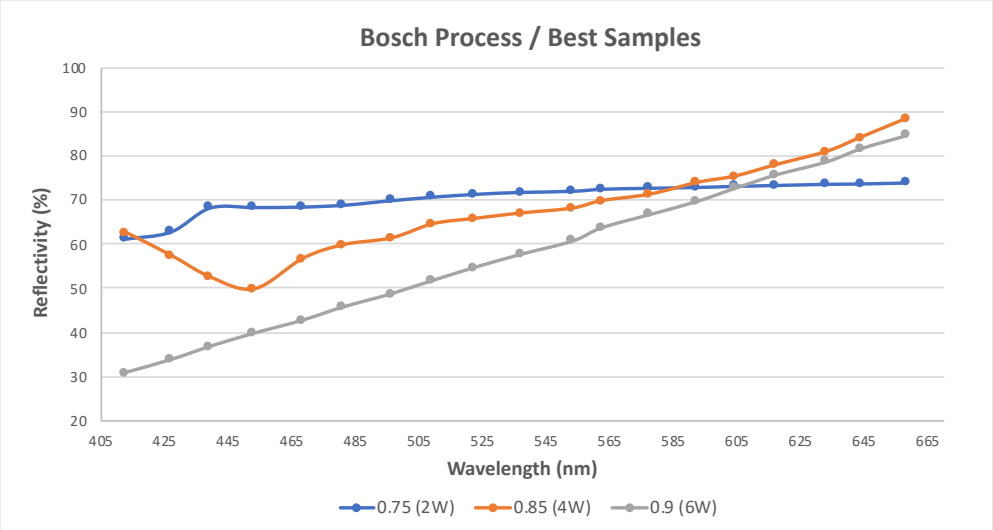

Figure 24. Reflectivity levels of best samples after Bosch process.

2.5.2. Water Contact Angle

To test the effect of applying the Bosch process, we used a water contact angle (WCA) test to measure the hydrophobic properties of the treated samples. Surprisingly, the setup revealed a significantly high contact angle for the Bosch-treated samples, while the samples with only black silicon showed almost no measurable contact angle. Initially, it was expected that the WCA test would also demonstrate hydrophobic properties in the untreated black silicon; however, the results indicated that the untreated black silicon did not exhibit hydrophobicity, whereas the Bosch-treated samples did. This difference may be attributed to the irregularity in the shape of the pillars in the untreated black silicon samples, likely caused by the large distances between the pillars in those samples.

Figure 25 shows the best black silicon sample treated at $\alpha = 0.85$ and 4 W. In this test, it was difficult to discern any distinct angle between the sample and the water surface, suggesting that this sample was hydrophilic. In contrast, Figure 26 illustrates a treated black silicon sample that exhibited a high level of hydrophobicity.

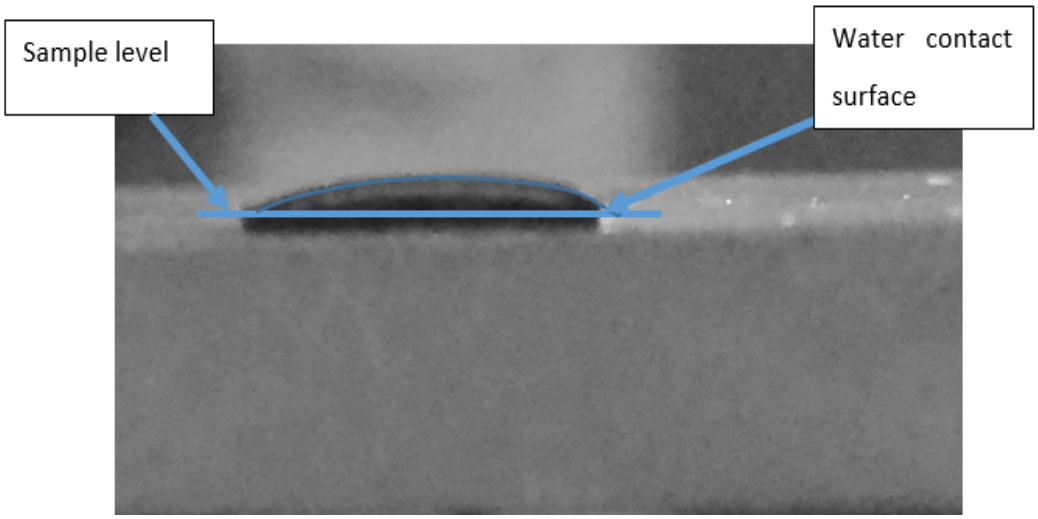

Figure 25. The hydrophobicity of a sample without the Bosch process.

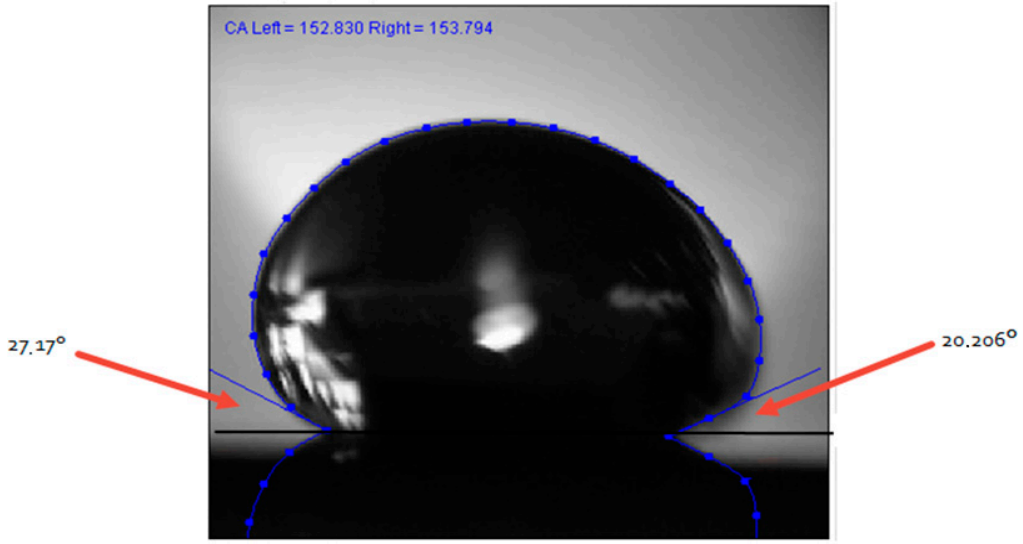

Figure 26. Hydrophobicity of sample treated with Bosch process.

3. Photovoltaic Cell Efficiency

In the previous sections, it was demonstrated that a higher density of microstructures, particularly those with conical and pillar-like shapes, leads to an improved refractive index. Additionally, to measure the electrical performance of b-Si-based photovoltaic cells, a few parameters are usually monitored and calculated. The fill factor (FF) is one of the important parameters used to determine the efficiency of a solar system [14]. The fill factor was calculated using Equation (4):

$$FF = \frac{V_{MP} \cdot I_{MP}}{V_{OC} \cdot I_{SC}} \quad (4)$$

where V_{OC} is the open-circuit voltage, I_{SC} is the short-circuit current, V_{MP} is the voltage value at the maximum power point, and I_{MP} is the current at the maximum power point.

The total efficiency (η) of the photovoltaic cell was calculated using Equation (5).

$$\eta = \frac{P_{out}}{P_{in}} \quad (5)$$

where P_{out} is the maximum electrical power output of the photovoltaic cell and P_{in} is the total incident optical power point. The maximum electric power output was calculated using Equation (6).

$$P_{out} = \frac{I_{SC} \cdot V_{OC} \cdot FF}{A} \quad (6)$$

where A is the area of the photovoltaic cell.

Table 5 depicts the calculated results for the fill factor and efficiency of the photovoltaic cell using the ICP RIE method.

Table 5. Efficiency results of photovoltaic cell.

Sample Fab. Method	V_m (V)	I_m (A)	V_{oc}	I_{sc}	FF	A (m^2)	P_{out} (W/m^2)	P_{in} (W/m^2)	η (%)
b-Si	0.585	0.318	0.622	0.364	0.822	0.0008	232.54	1000	23.25

Additionally, Table 6 presents performance data comparisons for different photovoltaic cell samples using different fabrication methodologies.

Table 6. Performance data comparisons for different photovoltaic cells.

Sample/Fabr. Method	V_{oc}	I_{sc}	FF (%)	H (%)
b-Si (ICP RIE)	0.622	0.364	82.2	23.3
b-Si (DRIE) [42]	0.665	0.422	78.7	22.1
b-Si (RIE) [43]	0.620	0.350	80.0	17.4
b-Si (PIII) [44]	0.621	0.320	78.3	15.7
b-Si (MACE) [45]	0.628	0.373	76.7	17.9
$SiO_2/WO_3/ZnO$ (80/20) [14]	0.437	0.207	48.5	5.48

In the table above, it can be seen that in our case the fill factor was higher (82.2%) compared to other fabrication methodologies for photovoltaic cells. Furthermore, black silicon (b-Si) photovoltaic cells achieved an efficiency of 23.3% with optimized nanostructures and effective passivation.

4. Results and Discussion

The results obtained from our experiments demonstrate important correlations between nanostructure geometry, hydrophobicity, and reflectivity that can improve the performance of b-Si photovoltaic cells. The fabrication procedures of black silicon were analyzed, and the factors influencing its reflectivity rate were evaluated. Various variables, including the gas ratio, the chuck bias power, and the application of the Bosch process, were carefully controlled. The goals were to achieve a low reflectivity level and to make the fabrication method more accessible and cost-effective for solar cell manufacturers. One of the key advantages of black silicon, in comparison to traditional grating techniques used in commercial solar cells, is its potential for lower-cost production.

The process began with the best-performing sample from the first stage ($\alpha = 0.9$) and progressed through a series of iterations with similar recipes: $\alpha = 0.75$ with a chuck bias of 2 W and $\alpha = 0.85$ with a chuck bias of 4 W. The 0.75 to 0.85 range was derived from a prior recipe that was shown to produce the best combination of the etching rate, surface structure, and material properties for photovoltaic cell efficiency. After conducting reflectivity tests, it was determined that the sample with $\alpha = 0.85$ exhibited the lowest reflectivity of 10% and 90% light absorption. The reflectivity measurements showed a marked decrease in surface reflectance, particularly in the UV and visible spectra, due to the nanostructured surface. Additional tests were performed, including hydrophobicity measurements to assess the water resistance properties of the b-Si layer.

Throughout the process, some challenges were encountered, particularly with reflectivity drops when creating a hydrophobic surface. Notably, the hydrophobic effect was more prominent in samples with short, thick, pillar-like structures, similar to the surface patterns found on lotus leaves. It was observed that the samples treated with the Bosch process exhibited structures resembling those produced by Bosch etching. For instance, the sample shown in Figure 26 demonstrated a contact angle of approximately 155°, which classified it as superhydrophobic. Furthermore, Figure 27 shows an image captured while testing the hydrophobic properties of black silicon.

The measurements derived from spectral reflectivity and the comparison of electrical performance indicate that the light absorption showed promising power output and efficiency. The results presented in Table 5 show a power output of 232.54 W/m^2 and an efficiency of approximately 23.3%, outperforming the other samples [14,42–45].

The results from the black silicon production and application study were generally close to the desired outcomes, as seen in the SEM images, reflectivity tests, and hydrophobicity measurements. While the reflectivity tests indicated some deterioration after applying the Bosch process, the best result in terms of low reflectivity was achieved with the sample with $\alpha = 0.85$ and a chuck bias of 4 W, as shown in Figure 28.

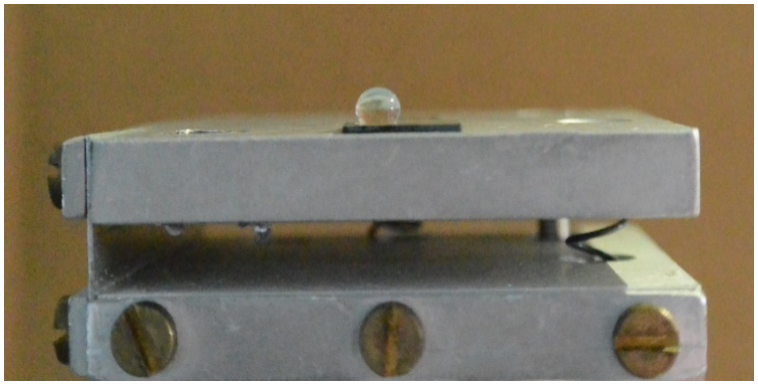

Figure 27. An image showing the hydrophobic properties of the treated black silicon.

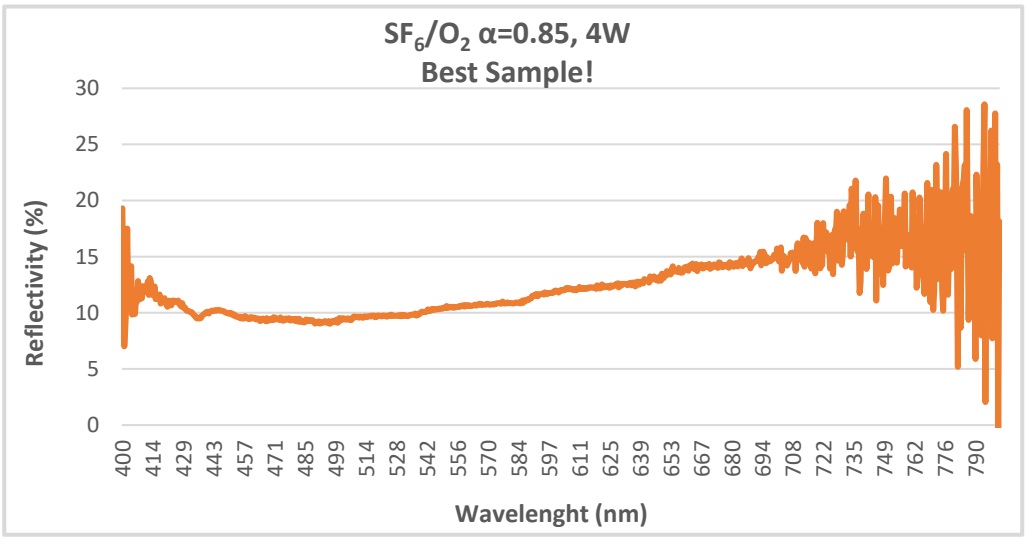

Figure 28. The lowest reflectivity rate achieved, about 10%, for the best sample with α = 0.85 and a chuck bias of 4 W.

5. Summary and Conclusions

In this research, we investigated the fabrication of an antireflection layer using the black silicon method. This was conducted in a cleanroom environment with an ICP RIE plasma etching system. This technique enabled the formation of nanostructures crucial for the antireflective layer applied to solar cells. The primary foci were to identify the most efficient fabrication process for these nanostructures and to explore the relationships between their size, geometry, and density and light absorption performance. The goal was to determine the optimal nanostructured shapes capable of more effectively harvesting photonic energy, thus enhancing charge generation (electron–hole pairs) and improving the electrical potential of solar cells when integrated into an array.

Fabrication of black silicon nanostructures was achieved through plasma etching, where ions generated in the plasma region bombarded a silicon surface. Two critical variables, the gas ratio (SF_6/O_2) and chuck bias power (W), were controlled to influence the bombardment rate, which directly impacted the size and shape of the nanostructures. By optimizing these parameters, nanostructures with high light absorption efficiency were successfully produced.

In the final stage, after refining the plasma etching parameters, samples with a reflectivity of 10% were obtained, corresponding to approximately 90% light absorption. However, several challenges arose during the process, including gas and power combinations that led to poor-quality black silicon or microstructures that did not significantly reduce reflectivity. Despite these setbacks, key parameters influencing the size, density,

and geometry of nanostructures critical for creating a high-quality black silicon layer were successfully identified. Additionally, the efficiency of the black silicon photovoltaic cell was 23.3%.

Several limitations were encountered, including constraints on the gas volume, power, etching time, and bombardment rate. The tests were conducted by varying one variable at a time while holding the others constant, a time-intensive approach essential for understanding the critical factors necessary for achieving low reflectivity. To optimize future results, computational models simulating light–matter interactions, coupled with control algorithms for process variables, could streamline the fabrication of high-quality antireflective layers.

The findings of this study offer promising insights into the key factors required to produce an effective antireflective layer for solar cells. The novelty of this method lies in its ability to improve the etching process by reducing costs, increasing scalability, and providing better control over surface morphology. Moreover, the results demonstrate that a clear understanding of the geometrical characteristics of nanostructures and their interactions with light can significantly enhance light absorption. This advancement opens the door for further optimization of the black silicon method, with the potential to develop more efficient, cost-effective solar cells that could become commercially viable for a broader range of consumers.

Author Contributions: Conceptualization, all authors; methodology, all authors; validation, K.D. and U.S.; investigation, U.S.; data curation, E.S.; writing—original draft preparation, K.D. and U.S. All authors have read and agreed to the published version of the manuscript.

Funding: This work was supported by the University of Southern Denmark NanoSYD; Tallinn University of Technology, Estonia; the University of Reading, Whiteknights, UK; and the Polytechnic University of Tirana, Albania.

Institutional Review Board Statement: Not applicable.

Informed Consent Statement: Not applicable.

Data Availability Statement: The data presented in this study are contained in this article.

Conflicts of Interest: The authors declare no conflicts of interest.

References

1. Khosal, S.; De, D.; Kar Ray, D.; Roy, T. Condition Monitoring of Fixed and Dual Axis Tracker using Curve Fitting Technique. *Int. J. Innov. Technol. Interdiscip. Sci.* **2023**, *6*, 1264–1272.
2. Dhoska, K.; Bebi, E.; Markja, I.; Milo, P.; Sita, E.; Qosja, S. Modelling the wind potential energy for metallurgical sector in Albania. *Sci. Rep.* **2024**, *14*, 1302. [CrossRef] [PubMed]
3. Marik, G.; Dutta, A. A Sustainable Evolution of Indian Railway. *J. Trans. Syst. Eng.* **2023**, *1*, 131–139.
4. Aubell, J.P.; Gebremedhin, A. Framed- or Frameless Photovoltaic in Snow Experiencing Climates. *Int. J. Innov. Technol. Interdiscip. Sci.* **2021**, *4*, 742–753.
5. Manfrinato, V.R.; Zhang, L.; Su, D.; Duan, H.; Hobbs, R.G.; Stach, E.A.; Berggren, K.K. Resolution Limits of Electron-Beam Lithography toward the Atomic Scale. *Nano Lett.* **2013**, *13*, 1555–1558. [CrossRef]
6. Zhou, H.; Chen, Q.; Li, G.; Luo, S.; Song, T.-B.; Duan, H.-S.; Hong, Z.; You, J.; Liu, Y.; Yang, Y. Interface engineering of highly efficient perovskite solar cells. *Science* **2014**, *345*, 542–546. [CrossRef]
7. Sökmen, U.; Stranz, A.; Fündling, S.; Wehmann, H.-H.; Bandalo, V.; Bora, A.; Tornow, M.; Waag, A.; Peiner, E. Capabilities of ICP-RIE cryogenic dry etching of silicon: Review of exemplary microstructures. *J. Micromech. Microeng.* **2009**, *19*, 105005. [CrossRef]
8. Dhoska, K.; Hofer, H.; Rodiek, B.; López, M.; Kübarsepp, T.; Kück, S. Improvement of the detection efficiency calibration and homogeneity measurement of Si-SPAD detectors. *Springerplus* **2016**, *5*, 2065. [CrossRef]
9. Deraoui, A.; Balhamri, A.; Rattal, M.; Younouss, B.; Abdelmoumen, T.; Harmouchi, M.; Mouhsen, A.; Oualim, E.M. Black Silicon: Microfabrication Techniques and Characterization for Solar Cells Applications. *Int. J. Energy Sci.* **2013**, *3*, 403–407. [CrossRef]
10. Pramono, A.; Dhoska, K.; Moezzi, R.; Milandia, A. Ti/SiC based metal matrix composites by using self-propagating high temperatures synthesis (SHS). *Rev. Des Compos. Des Matériaux Avancés-J. Compos. Adv. Mater.* **2021**, *31*, 125–129. [CrossRef]
11. Gorshkov, V.N.; Stretovych, M.O.; Semeniuk, V.F.; Kruglenko, M.P.; Semeniuk, N.I.; Styopkin, V.I.; Gabovich, A.M.; Boiger, G.K. Hierarchical Structuring of Black Silicon Wafers by Ion-Flow-Stimulated Roughening Transition: Fundamentals and Applications for Photovoltaics. *Nanomaterials* **2023**, *13*, 2715. [CrossRef] [PubMed]

12. Pramono, A.; Dhoska, K.; Markja, I.; Kommel, L. Impact pressure on mechanical properties of aluminum-based composite by ECAP-parallel channel. *Pollack Period.* **2019**, *14*, 67–74. [CrossRef]
13. Golubewa, L.; Rehman, H.; Padrez, Y.; Basharin, A.; Sumit, S.; Timoshchenko, I.; Karpicz, R.; Svirko, Y.; Kuzhir, P. Black Silicon: Breaking through the Everlasting Cost vs. Effectivity Trade-Off for SERS Substrates. *Materials* **2023**, *16*, 1948. [CrossRef] [PubMed]
14. Koysuren, O.; Dhoska, K.; Koysuren, H.N.; Markja, I.; Yaglikci, S.; Tuncel, B. $SiO_2/WO_3/ZnO$ based self-cleaning coatings for solar cells. *J. Sol-Gel Sci. Technol.* **2024**, *110*, 183–203. [CrossRef]
15. Tyxhari, G.; Gorishti, A.; Dhoska, K. Energy Audit Evaluation in the Private Residential Building. *Int. J. Tech. Phys. Probl. Eng.* **2023**, *15*, 294–298.
16. Trabelsi, A.B.G.; Kaliyannan, G.V.; Gunasekaran, R.; Rathanasamy, R.; Palaniappan, S.K.; Alkallas, F.H.; Elsharkawy, W.; Mostafa, A.M. Surface engineering of Sio_2-Zro_2 films for augmenting power conversion efficiency performance of silicon solar cells. *J. Mater. Res. Technol.* **2024**, *28*, 1475–1482. [CrossRef]
17. Dhoska, K.; Dumishllari, E.; Sulejmani, A.; Çejku, M.; Koça, O. Assessing energy consumption in private residential building area. *Int. J. Mech. Control* **2024**, *25*, 3–8.
18. Pramono, A.; Nežerenko, O.; Fitrullah, M.; Suryana. Microstructural Evolution and Mechanical Properties Enhancement of Ti/SiC Metal Matrix Composites. *J. Trans. Syst. Eng.* **2024**, *2*, 295–305.
19. Steglich, M.; Käsebier, T.; Zilk, M.; Pertsch, T.; Kley, E.B.; Tünnermann, A. The structural and optical properties of black silicon by inductively coupled plasma reactive ion etching. *J. Appl. Phys.* **2014**, *116*, 173503. [CrossRef]
20. Alsolami, A.; Hussain, H.; Noor, R.; AlAdi, N.; Almalki, N.; Kurdi, A.; Tabbakh, T.; Zaman, A.; Alfihed, S.; Wang, J. Recent Advances in Black Silicon Surface Modification for Enhanced Light Trapping in Photodetectors. *Appl. Sci.* **2024**, *14*, 9841. [CrossRef]
21. Schmelz, D.; Käsebier, T.; Shi, Z.; Cheng, Q.; Sergeev, N.; Schelle, D.; Zeitner, U. Investigations on black silicon nanostructures fabricated by reactive ion etching on highly curved surfaces. *Mater. Sci. Semicond. Process.* **2023**, *165*, 107646. [CrossRef]
22. Zhang, X.; Li, W.; Jin, C.; Cao, Y.; Liu, F.; Wei, N.; Wang, B.; Zhou, R.; Zhu, X.; Zhao, W. Effects of Black Silicon Surface Morphology Induced by a Femtosecond Laser on Absorptance and Photoelectric Response Efficiency. *Photonics* **2024**, *11*, 947. [CrossRef]
23. Padrez, Y.; Golubewa, L. Black Silicon Surface-Enhanced Raman Spectroscopy Biosensors: Current Advances and Prospects. *Biosensors* **2024**, *14*, 453. [CrossRef] [PubMed]
24. Algethami, F.K.; Trabelsi, K.; Hajjaji, A.; Rabha, M.B.; Khezami, L.; Elamin, M.R.; Bessais, B.; El Khakani, M.A. Photocatalytic Activity of Silicon Nanowires Decorated with PbS Nanoparticles Deposited by Pulsed Laser Deposition for Efficient Wastewater Treatment. *Materials* **2022**, *15*, 4970. [CrossRef] [PubMed]
25. Chai, J.Y.-H.; Wong, B.T.; Juodkazis, S. Black-silicon-assisted photovoltaic cells for better conversion efficiencies: A review on recent research and development efforts. *Mater. Energy* **2020**, *18*, 100539. [CrossRef]
26. Vorobyev, A.Y.; Guo, C. Direct creation of black silicon using femtosecond laser pulses. *Appl. Surf. Sci.* **2011**, *257*, 7291–7294. [CrossRef]
27. Venkatesan, R.; Arivalagan, M.K.; Venkatachalapathy, V.; Pearce, J.M.; Mayandi, J. Effects of silver catalyst concentration in metal assisted chemical etching of silicon. *Mater. Lett.* **2018**, *221*, 206–210. [CrossRef]
28. Colniţă, A.; Marconi, D.; Brătfălean, R.T.; Turcu, I. Single-step fabrication of homoepitaxial silicon nanocones by molecular beam epitaxy. *Appl. Surf. Sci.* **2018**, *436*, 1163–1172. [CrossRef]
29. Ramos, C.; Verduzco-Lopez, Y.; Alvarez-Macias, C.; Sanchez-Juarez, A.; Dutt, A.; Santana, G. A new passivation scheme for the performance enhancement of black silicon solar cells. *Mater. Today Commun.* **2019**, *20*, 100556. [CrossRef]
30. Atteia, F.; Le Rouzo, J.; Berginc, G.; Simon, J.J.; Escoubas, L. Black silicon (BS) using room-temperature reactive ion etching (RT-RIE) for interdigitated back contact (IBC) silicon solar cells. In Proceedings of the SPIE 10913, Physics, Simulation, and Photonic Engineering of Photovoltaic Devices, San Francisco, CA, USA, 5–7 February 2019; Volume VIII, p. 109130U.
31. Broers, A.N.; Hoole, A.C.F.; Ryan, J.M. Electron beam lithography—Resolution limits. *Microelectron. Eng.* **1996**, *32*, 131–142. [CrossRef]
32. Chou, S.Y. Sub-10 nm imprint lithography and applications. *J. Vac. Sci. Technol. B Microelectron. Nanom. Struct* **1997**, *15*, 2897. [CrossRef]
33. Vaseashta, A.; Dimova-Malinovska, D. Nanostructured and nanoscale devices, sensors and detectors. *Sci. Technol. Adv. Mater* **2005**, *6*, 312–318. [CrossRef]
34. Randolph, S.J.; Fowlkes, J.D.; Rack, P.D. Focused, Nanoscale Electron-Beam-Induced Deposition and Etching. *Crit. Rev. Solid State Mater. Sci.* **2006**, *31*, 55–89. [CrossRef]
35. Shul, R.; Vawter, G.; Willison, C.; Bridges, M.; Lee, J.; Pearton, S.; Abernathy, C. Comparison of plasma etch techniques for III–V nitrides. *Solid. State. Electron* **1998**, *42*, 2259–2267. [CrossRef]
36. Dry Etching (ICP RIE)-NanoSYD Cleanroom. Available online: https://www.sdu.dk/en/samarbejde/forskere/faciliteter/teklaboratorier/cleanroom (accessed on 27 May 2024).
37. Jansen, H.; de Boer, M.; Burger, J.; Legtenberg, R.; Elwenspoek, M. The black silicon method II: The effect of mask material and loading on the reactive ion etching of deep silicon trenches. *Microelectron. Eng.* **1995**, *27*, 475–480. [CrossRef]
38. Chang, C.; Wang, Y.-F.; Kanamori, Y.; Shih, J.-J.; Kawai, Y.; Lee, C.-K.; Wu, K.-C.; Esashi, M. Etching submicrometer trenches by. Etching submicrometer trenches by using the Bosch process and its application to the fabrication of antireflection structures. *J. Micromech. Microeng.* **2005**, *15*, 580. [CrossRef]

39. Scanning Electron Microscope-NanoSYD Cleanroom. Available online: https://www.sdu.dk/en/samarbejde/forskere/faciliteter/teklaboratorier/structural_test_lab (accessed on 9 May 2024).
40. Determination of Contact Angle from Contact Area of Liquid Droplet Spreading on Solid Substrate from Leonardo Electronic Journal of Practices and Technologies. Available online: http://lejpt.academicdirect.org/A10/029_038.htm (accessed on 10 May 2024).
41. Oh, J.; Yuan, H.-C.; Branz, H.M. An 18.2%-efficient black-silicon solar cell achieved through control of carrier recombination in nanostructures. *Nat. Nanotechnol.* **2012**, *7*, 2–5. [CrossRef]
42. Savin, H.; Repo, P.; von Gastrow, G.; Ortega, P.; Calle, E.; Garín, M.; Alcubilla, R. Black silicon solar cells with interdigitated back-contacts achieve 22.1% efficiency. *Nat. Nanotechnol.* **2015**, *10*, 624–628. [CrossRef] [PubMed]
43. Yoo, J.; Cho, J.-S.; Ahn, S.; Gwak, J.; Cho, A.; Eo, Y.-J.; Yun, J.-H.; Yoon, K.; Yi, J. Random reactive ion etching texturing techniques for application of multicrystalline silicon solar cells. *Thin Solid Film.* **2013**, *546*, 275–278. [CrossRef]
44. Xia, Y.; Liu, B.; Liu, J.; Shen, Z.; Li, C. A novel method to produce black silicon for solar cells. *Sol. Energy* **2011**, *85*, 1574–1578. [CrossRef]
45. Kim, C.; Lee, J.; Lim, S.; Jeong, C. Enhanced absorption and short circuit current density of selective emitter solar cell using double textured structure. *Sol. Energy* **2015**, *116*, 265–271. [CrossRef]